Title: Dynamic nuclear lamina-chromatin interactions during G1 progression

Authors: Joseph R. Tran[1], Stephen A. Adam[2], Robert D. Goldman[2] and Yixian Zheng[1,3]

Affiliations:
1. Carnegie Institution for Science, Department of Embryology, 3520 San Martin Drive, Baltimore, MD 21218.
2. Northwestern University, Feinberg School of Medicine, Department of Cell and Developmental Biology, Ward Building 11-145, 303 E. Chicago Ave. Chicago, IL 60611
3. To whom correspondence should be addressed: tran@carnegiescience.edu, zheng@carnegiescience.edu

Running head:
Nuclear lamina-chromatin interaction during G1 progression

Keywords:
Nuclear lamina, lamin, TSA-seq, mitosis, G1, senescence, cell cycle, lamina-associated domains, LADs, SLAM-seq

Abstract

A large fraction of heterochromatin in the metazoan genome is associated with the nuclear lamina (NL) in interphase nuclei. This heterochromatin is often referred to as Lamina-Associated Domains (LADs) and are often mapped from cell populations asynchronously progressing through the cell cycle. We and others have recently reported that LADs are largely stable during G1, S, or G2 phases of the cell cycle, and appear similar to LADs mapped from bulk cell populations. LADs in senescent cells, however, are reported to be quite different from proliferating cells, and it remains unclear how senescent cell LADs are established. As cells finish mitosis and re-enter G1, reassembly of the nuclear envelope and NL appears to precede mitotic chromosome decondensation. Therefore, the initial NL interactions with the decondensing chromatin may be quite different from those reported in asynchronous or FACS isolated G1, S, or G2 populations. By developing a modified version of the Tyramide-Signal Amplification sequencing (TSA-seq), which we call chromatin pull down-based Tyramide Signal Amplification-sequencing (cTSA-seq), we uncover a dynamic NL-chromatin interaction as cells progress through G1. The appearance of stable LADs coincides with sufficient chromatin decondensation and active gene expression in G1. Interestingly, early G1 NL-chromatin interactions, which are found toward the telomeric ends of human chromosomes, are similar to those found in oncogene-induced senescent cells. We find that the assembly of LADs during the formation of the G1 nucleus is gradual and that the arrest of NL-chromatin interactions in early G1 may contribute to genome disorganization of senescence cells.

Introduction

A portion of the genome is organized into compact, transcriptionally-repressive DNA known as heterochromatin. A large fraction of heterochromatin in the metazoan cell nucleus is localized to the nuclear periphery and proximal to the nuclear lamina (NL). The NL is a complex meshwork composed of filamentous A- and B-type lamins that underlies the nuclear envelope (NE) and the heterochromatic regions associated with the NL are known as lamina-associated domains (LADs) (Chen et al., 2018; Guelen et al., 2008). Most studies of LADs have been performed using asynchronously dividing cell cultures, and represents an averaged NL-chromatin interaction across all phases of the cell cycle. Recently, we and others have mapped G1, S, and G2/M phase LADs from cells FACS sorted by their DNA content (Tran et al., 2020; van Schaik et al., 2019). These maps revealed fairly small variations in LADs among the three cell cycle stages, and indicated that LADs in G1, S, and G2 phases are largely stable (Tran et al., 2020; van Schaik et al., 2019).

After mitosis, the nuclear envelope begins to reassemble in telophase with NL components such as lamin-B1, BAF, Lap2α and Emerin assembling onto the post mitotic chromosomes that continue to decondense (Dechat et al., 2004; Haraguchi et al., 2008; Haraguchi et al., 2001; Moir et al., 2000b). Since the FACS-isolated 2N cells from asynchronously dividing cell populations represent a mixture of different stages of G1, the LADs mapped in this asynchronous G1 cell population may not identify NL-chromatin interactions during the early G1 phase when chromatin is not fully decondensed.

Indeed, studies suggest that the post-mitotic genome is spatially dynamic in early interphase but becomes more stable later in the cell cycle (Chubb et al., 2002; Croft et al., 1999; Thomson et al., 2004; Walter et al., 2003). For example, telomeres are transiently enriched at the nuclear periphery in early G1 prior to redistribution throughout the nucleus (Crabbe et al., 2012), and studies of the heterochromatic homogeneously staining region in Chinese Hamster Ovary cells have reported early G1 dynamism of this region prior to compaction and localization at the nuclear periphery (Li et al., 1998). Furthermore, DamID-m6A tracer studies have observed the relocation of some m6A marked LADs from the nucleoplasm during early G1 to a more NL-proximal localization (Kind et al., 2013; Luperchio et al., 2018). These observations raise the possible temporal sequence where the distal ends of chromosomes transiently localize near the NL in early G1 followed by re-organization and formation of the relatively stable G1 LADs that are similar to LADs found in S and G2 phases. Additionally, as chromosomes continue their decondensation during early G1, only the exposed chromatin surface may interact with the NL. Therefore, reorganization of NL-chromatin interactions may continue when more and more LAD regions are exposed as chromatin returns to its interphase state. Understanding how post mitotic cells initiate NL-chromatin interactions and how such interactions are modified to achieve a stable LAD pattern is important because it will shed light on how a normal or defective interphase genome organization is established.

To probe how the NL interacts with chromatin as cells return to and progress through G1 phase, an NL-genome mapping method capable of high temporal resolution is required. LADs are commonly mapped by three main methods: chromatin-

immunoprecipitation (ChIP)-seq, DNA adenine methyltransferase identification (DamID) and Tyramide Signal Amplification-sequencing (TSA-seq) (Chen et al., 2018; Dou et al., 2015; Forsberg et al., 2019; Guelen et al., 2008). However, some limitations of these methods, such as insolubility of NL and temporal resolution of labeling, preclude their use for efficient mapping of LADs in early G1. Recently, we adapted the Ascorbate Peroxide identification (APEX2-ID) method, which APEX2 was expressed as a fusion protein with lamin-B1, to temporally map LADs during the cell cycle (Tran et al., 2020). However, the APEX2-ID method has its own limitations, such as variable transfection efficiency in different cells and unwelcomed overexpression effects. The van Steensel group recently developed a technology to map cell cycle LADs using an antibody-targeted DamID approach highlighting a convergence toward antibody-based methods (van Schaik et al., 2019).

The TSA-seq genome mapping method, described by the Belmont group (Chen et al., 2018), is attractive as it allows the user to temporally resolve events based on the timing of cellular fixation. TSA-seq uses common reagents familiar to most biochemical and molecular biology labs and is in essence an antibody-staining assay. The protocol uses horseradish peroxidase (HRP) to covalently attach biotin onto nearby proteins and DNA (Chen et al., 2018). Furthermore, the TSA-seq reaction allows labeling of essentially any endogenously expressed proteins of interest, thus mitigating the issues associated with transfection variability. However, the biotinylation of DNA is inefficient and the assay requires a large number of cells which are not easily obtained for some types of temporal studies. Therefore we have developed a chromatin pull down-based TSA-seq method, which we call cTSA-seq, to study lamin-B1-genome interaction

dynamics as cells progress through the G1 phase of the cell cycle. We find that lamin B1-genome interactions are first restricted to the telomeric distal ends of chromosomes in early G1 followed by the adoption of a profile typically observed as LADs throughout the rest of the cell cycle. We show that LADs mapped from the oncogene-induced senescence model (Lenain et al., 2017; Sadaie et al., 2013) are similar to LADs found in early G1. Our findings have significant implications for the understanding of genome organization in dividing cells and cells undergoing senescence.

Materials and Methods

Cell culture

HCT116 (ATCC, #CCL-247), GM12878 (Coriell, #GM12878), K562 (ATCC, #CCL-243) and hTERT-RPE-1 (ATCC #CCL-4000) were cultured in McCoy's 5a with 10% FBS (HCT116), RPMI media with 15% (GM12878), IMDM media with 15% (K562), DMEM-F12 with 15% (hTERT-RPE-1), and DMEM (mouse embryonic fibroblast) supplemented with 15% FBS, respectively. Mouse embryonic stem cells were cultured in 2i media. HCT116 and hTERT-RPE-1 were cultured in 100 or 150mm dishes. GM12878 and K562 cells were cultured in T25 and T75 flasks, respectively. Mouse embryonic stems cells were cultured feeder-free in gelatinized 6-well plates. All cells were cultured at 37 °C in 5% CO_2.

Nocodazole block, release and harvest for early and later G1 cells

HCT116 or hTERT-RPE-1 cells were cultured in three 150mm dishes to ~40-60% confluency per experiment and then exposed to nocodazole (100ng/ml) for 18 hours. The cells were washed two times with 10 ml of pre-warmed media and mitotic cells were shaken off and seeded onto 100mm dishes that were pre-coated with poly-lysine. A fraction of the shake-off cells was saved and fixed with 1% paraformaldehyde for 10 minutes at room temperature to check for purity of the shake-off population by FACS (see below). The seeded cells were harvested at the indicated post-seeding times by trypsinization and then immediately fixed with 1% paraformaldehyde for 10 minutes at room temperature. For experiments with G1, S, and G2 phases, asynchronous cultures were harvested by trypsinization and fixed for 10 minutes with 1% paraformaldehyde.

Paraformaldehyde fixation was neutralized with 125mM glycine and the cells were pelleted at 300g x 5 minutes and washed with phosphate buffered saline (PBS).

Fluorescence Activated Cell Sorting (FACS) to analyze and isolate cells at different stages of cell cycle

All FACS was performed on a BD FACSaria III machine and on average we obtained 800,000 to 1 million cells unless noted otherwise.

For FACS of cell cycle stage-specific populations, nocodazole block and released cells or asynchronous cells were fixed as described above and resuspended in HBSS + 2% FBS + 10μg/ml Hoechst 33342. The cells were incubated with Hoechst 33342 for at least 20 minutes at room temperature before FACS for G1, S and G2/M. For nocodazole block and release, we rejected samples where the shake-off mitotic population contained greater than 1% of contaminating G1 cells.

For SLAM-seq experiments (see section, “Thiol (SH)-Linked Alkylation for the Metabolic sequencing of RNA” below), FACS based cell isolation was done with live cells stained with 10μg/ml Hoechst 33342 in the last 20 minutes of culture. Sorting was done for a maximum of 10 minutes in order to limit time in suspension and this generally yielded between 30,000 to 100,000 cells for SLAM-seq.

Chromatin pull down-based TSA-seq (cTSA-seq)

Paraformaldehyde (1%)-fixed cell populations were permeabilized with PBS containing 0.25% Triton X-100 for 10 minutes at room temperature. Permeabilized cells were pelleted at 200g x 5 minutes and the supernatant was carefully removed using a P100 pipette. The cells were then resuspended in PBS + 1% hydrogen peroxide and incubated for 20 minutes at room temperature to neutralize endogenous peroxidases.

The suspension was then pelleted at 200g x 5 minutes and carefully aspirated with a P100 pipette. The cells were blocked for 20 minutes in PBS containing 10% normal goat serum, 10% BSA and 10mM sodium azide and pelleted as described above. The cells were resuspended by gently flicking the tube in the same blocking buffer containing 1:250 dilution of rabbit anti-Lamin B1 antibody (Abcam, #ab16048) and incubated overnight at 4 °C in a microfuge tube rack. The following day, the cells were pelleted at 200g x 5 minutes and carefully aspirated with a P100 pipette. The pellet was washed 2 x 15 minutes with PBS supplemented with 0.001% Tween-20. The secondary and TSA reaction reagents were from a commercial Biotin-XX-Tyramide Superboost kit (Invitrogen, #2005939) and were used as follows. The primary antibody stained cells were resuspended by gently flicking in ~100μl of the provided anti-rabbit HRP secondary antibody solution and incubated in a microfuge tube rack at room temperature for 2 hours with intermittent mixing. The cells were pelleted at 200g x 5 minutes, washed 3 x 15 minutes with PBS + 0.001% Tween-20 and one time with 1x reaction buffer supplied with the biotin tyramide kit. The reaction was performed as described for the Biotin-XX-Tyramide Superboost kit with only one modification. The reaction was incubated in an Eppendorf Thermomixer set to 25 °C with 300 rpm shaking for 10 minutes. The reaction was neutralized by adding PBS + 10mM sodium ascorbate, 10mM Trolox and 10mM sodium azide to halt HRP activity and pelleted at 200g x 5 minutes. The cells were resuspended in PBS + 0.001% Tween-20 by flicking. A small aliquot was taken to confirm the reaction by fluorescence staining (see below) and the remainder was pelleted and stored at -80 °C or immediately used for Streptavidin pull-down (see below).

Fluorescence staining for the cTSA-seq reaction

Cells from the completed cTSA-seq reaction were resuspended in PBS containing 0.001% Tween-20 and Streptavidin conjugated to Alexa 488 (1:200, Biolegend, #405235) and an anti-rabbit secondary conjugated (1:1000) to an Alexa 594 fluorophore. The cells were then stained with DAPI and mounted in Prolong anti-fade gold for imaging on a Leica SP5 scanning confocal microscope using the Leica Application Suite v2.7.3.9723. We used a 40x 1.4NA objective with Leica Type F immersion oil.

Streptavidin pull-down of lamina-associated chromatin

The cells were resuspended in 300μl RIPA buffer (50 mM Tris, 150 mM NaCl, 0.1% (wt/vol) SDS, 0.5% (wt/vol) sodium deoxycholate and 1% (vol/vol) Triton X-100, pH 7.5) supplemented with phenylmethylsulfonyl fluoride (PMSF) and incubated at 4 °C with end-over-end rotation for 30 minutes. The suspension was sonicated on a Diagenode Bioruptor Pico and a 50μl aliquot of the resulting lysate was collected for the input while the remainder was used for the pull-down portion of the pulldown experiment. The input was digested with 10μl of 10mg/ml Proteinase K overnight at 50 °C with 700 rpm shaking. For the Streptavidin pull-down (StrePD), Streptavidin coated magnetic beads (Pierce, #88817) were washed and resuspended in RIPA buffer. We added ~70μl of Streptavidin beads per pull-down. The following day, the magnetic beads were collected and washed sequentially with 2 x 1ml RIPA, 1 x 1ml LiCl buffer (250mM LiCl, 1% IGEPAL-CA630, 1% deoxycholic acid, 10mM Tris, pH 8.0, 1mM EDTA), 1 x 1ml with high salt buffer (1M KCl, 50mM Tris-Cl pH 8.0, 5mM EDTA), 1 x

1ml Urea wash buffer (2M Urea, 10mM Tris-Cl pH 8.0), and then 1 x 1ml RIPA. The beads were resuspended in 50μl RIPA buffer and digested with 5μl of 10mg/ml Proteinase K overnight at 50 °C with 700 rpm shaking. The input and StrePD DNA were purified using Ampure XP beads (Agencourt).

Thiol (SH)-Linked Alkylation for the Metabolic sequencing of RNA (SLAM-seq)

To determine new transcription for FACS isolated unsynchronized G1 (from asynchronous cell culture) or synchronized early and later G1 cells, we incubated asynchronous HCT116 cultures or re-seeded mitotic shake-offs of HCT116 cells with 500μM 4-thiouridine (4sU) for 1 hour prior to harvest. Twenty minutes before harvest, we pre-stained cellular DNA by directly adding Hoechst 33342 to a final of 10μg/ml. The cells were harvested by trypsinization, pelleted at 150g x 3 minutes and resuspended in HBSS + 2% FBS supplemented with 10μg/ml Hoechst 33342 that was pre-warmed to 37 °C. The cells were immediately filtered with a 0.45 micron filter and FACS analyzed as described above with the exception that the cell sorting chamber was also set to 37 °C since the cells were alive. FACS was performed for a maximum of 10 minutes, which usually yielded anywhere between 30,000 and 100,000 cells. The collected cells were then pelleted at 500g x 3 minutes, aspirated with a P100 pipette and RNA was immediately extracted using the Qiagen RNeasy Plus kit and quantitated. To convert the incorporated 4sU, we incubated the RNA (~0.5-1μg) in PBS pH 7.4 with 100μM iodoacetamide at 50 °C for 15 minutes and then re-purified the RNA using the Qiagen RNeasy Plus kit.

Sequencing library production

RNA library building was done using the Illumina TruSeq RNA library kit v2 with Ribo-depletion. DNA libraries were prepared using the Rubicon Genomics ThruPlex kit. Sequencing was performed on the Illumina NextSeq 500 platform.

Data processing

LADs mapping was done by aligning input and StrePD reads using the hg19 or mm9 assemblies with Bowtie 2.3.2 under the default setting. Duplicates were removed using Samtools v1.6. The reads were then called into 10 or 100 kilobase (kb) genomic windows using the coverage function in Bedtools v2.26.0. Next, we normalized the StrePD and input read count data to one million, calculated the StrePD/input ratio by log2 and transformed the data to a z-score. K562 cell DamID and TSA-seq LADs data (Chen et al., 2018) was obtained from Gene Expression Omnibus (GEO) GSE66019, the K562 cell APEX2-ID data (Tran et al., 2020) was from GEO GSE159482, the Tig3 OIS data (Lenain et al., 2017) was obtained from GEO SE76605, IMR90 OIS data (Sadaie et al., 2013) was obtained from GEO GSE49341 and the epigenome data for HCT116 cells was obtained from the ENCODE project (HCT116 reference epigenome series ENCSR361KMF). The publicly available LADs and lamin-B1 ChIPseq datasets were called into 100kb windows and treated as above. The depmixS4 v1.4-0 R package was used to call a three-state Hidden Markov Model (HMM) to identify LADs coordinates. We intersected the HMM calls between experimental replicates to find LAD regions that were reproducibly identified. Quantitation of epigenetic and lamin-B1 signals was done using the bigwigAverageOverBed from the Kentutils v3.62 package. For analyses that examined chromosomes as a percentage of their length, we first split

chromosomes in 200 windows using the makewindows function in bedtools and then quantitated the lamin-B1 signal over these windows using the bigwigAverageOverBed function from Kentutils. Additional analysis, statistics and graphical plotting were done either in R Studio v0.98.95.3 using the pHeatmap v1.0.12, corrplot v0.84, Hmisc v4.2-0, and depmixs4 v1.4-0 packages or Microsoft Excel 2016. Browser tracks were displayed using the UCSC Genome Browser with a smoothing window of 2.

For SLAM-seq experiments reads were initially trimmed by 10 nucleotides from both the 5' and 3' ends using cutadapt v1.6. The trimmed RNA-seq data was aligned with Bowtie 2.3.2 and Tophat2 under default settings using the Ensembl hs75 assembly. Polymorphisms corresponding to the expected U- to C-conversions were quantitated using the GrandSLAM v 2.0.5c package (Jurges et al., 2018). Data was filtered for a minimum of 10 transcripts per million (TPM) and the new to total RNA (NTR, "MAP") value was used to represent the gene for subsequent analysis. Statistics and graphical plotting were done either in R Studio v0.98.95.3 using base functions, pHeatmap v1.0.12, corrplot v0.84, car v3.0-5 and Hmisc v4.2-0 packages, or Microsoft Excel 2016.

Results and discussion

Chromatin pull down-based Tyramide Signal Amplification-sequencing (cTSA-seq) reliably maps LADs

TSA-seq has been used to map genomic structures and has found utility as a molecular ruler to measure distances between genomic structures (Chen et al., 2018; Zhang et al., 2019). To test the Tyramide Signal Amplification (TSA) labeling of the NL, we performed TSA reactions on different cell lines, K562, HCT116, or mouse embryonic fibroblasts (MEFs) (Figure 1A) with a rabbit lamin-B1 antibody. Post-reaction staining for Streptavidin coincided with the lamin-B1 in these cell as expected, but not in control reactions that either omitted the hydrogen peroxide, used an anti-mouse horseradish peroxidase secondary antibody or in lamin-B1 null MEFs (Figure 1B, S1A, S1B). Similar to previous work (Chen et al., 2018), diffusion of biotin labeling from the unmodified TSA reaction was ~1 μm on average from the lamin-B1 antibody signal (Figure S1C).

The TSA-seq method has a number of technical advantages, including the labeling of all cells that endogenously express a given protein. However, the reliance on pulling down the low level of biotinylated DNA necessitates the use of 10-1000 millions of cells (Chen et al., 2018; Zhang et al., 2020) and this makes the genomic mapping of low abundance cells, such as the G1 synchronized cells, quite challenging. We therefore examined whether or not pulling down the fragmented biotinylated chromatin using streptavidin beads (Figure 1A) could be used to map LADs. We refer, hereafter, to this method as chromatin pull down-based TSA-sequencing (cTSA-seq) and performed lamin-B1 cTSA-seq on K562 cells. The cells were lysed, and after chromatin fragmentation by sonication, the entire lysate was subject to Streptavidin bead pull-

down (StrePD). Input and StrePD DNA samples were sequenced and mapped to the hg19 genome assembly. Biological replicates of LAD profiles obtained by the cTSA-seq method were reproducible (Figure S1D, Pearson = 0.93) and the average signal was both visually (Figure 1C, left) and statistically similar to those obtained by DamID, the original TSA-seq method and our recently adapted APEX2-ID method in K562 cells (Figure 1C, right). cTSA-seq identified 97.3% of TSA-seq LADs defined by Hidden Markov Model (HMM). The high correlation among cTSA-seq, TSA-seq, DamID, and APEX-ID shows that cTSA-seq is a complementary tool to TSA-seq that efficiently identifies NL-chromatin interactions that are dominantly composed of LADs from 800,000 to 1 million cells.

Isolation of cells from early or later G1 phase based on nocodazole block and release as judged by immunostaining and by sequencing newly transcribed mRNAs

In order to examine NL-chromatin interactions during early and later G1, we first used nocodazole to arrest HCT116 cells for 16 hours. The mitotic cells were shaken off, washed and reseeded (Figure 2A). FACS analyses showed that HCT116 cells released from nocodazole synchronously progressed into G1 and S phases of the cell cycle (Figure 2B). A clear 2N G1 cell peak could be seen between 60-90 minutes after release, and by 180-240 minutes the DNA profile appeared similar to that seen for asynchronous cultures (Figure 2B), suggesting that much of the cell population had finished mitosis and progressed into interphase.

To more clearly assess HCT116 cells that entered G1 after nocodazole release, we used FACS to isolate the 2N cells at 90 or 180 minutes after release followed by

immunostaining for lamin-B1. These cell populations will be referred to as 90m or 180m G1 cells, respectively, to differentiate them from the asynchronous 2N G1 cells isolated by FACS from asynchronous cell populations ("Async G1"). We found that both 90m and 180m G1 cells have interphase nuclei with fully assembled NL and nuclear envelope as judged by lamin-B1 staining (Figure 2C). By examining DAPI staining of DNA, however, we noticed that the chromatin in most 90m G1 nuclei appeared to not be fully decondensed, whereas nuclei in the 180m G1 cells had largely decondensed chromatin in manner similar to many asynchronously growing G1 HCT116 cells (Figure 2C, 2D). This progressive chromosome decondensation in G1 was previously observed for synchronized cells released from mitotic block (Belmont and Bruce, 1994). Using the same nocodazole block and release protocol, we can similarly isolate early (90m) or later (180m) G1 hTERT-RPE1 cells. Based on the FACS profile, the hTERT-RPE1 cells appeared to progress through G1 and S phases slower than that of HCT116 cells (Figure S2A). However, similar to HCT116 cells, staining of FACS-isolated hTERT-RPE1 cells revealed that the lamina was reformed and DNA was not fully condensed at 90 minutes into G1 (Figure S2B).

To further confirm that the 90m and 180m cells we obtained using the above synchronization and FACS procedure represented the early and later stages of G1, respectively, we employed the Thiol (SH)-Linked Alkylation for the Metabolic sequencing of RNA (SLAM-seq) labeling strategy (Figure S2C) to measure active transcription (Herzog et al., 2017) as cells enter G1. Cells treated with 4-thiouridine (4sU) incorporate the analog into newly transcribed RNA (Dolken, 2013). Total RNA, which contains the fraction labeled with 4sU, was treated with iodoacetamide. This

modification results in a U- to C-conversion during reverse transcription and these conversions can be quantitated and expressed as a new RNA transcripts to total RNA ratio (NTR) using the GRAND-SLAM package (Erhard et al., 2019; Herzog et al., 2017). We performed SLAM-seq of the 90m G1, 180m G1, and asynchronous G1 samples by labeling with 4sU for 60 minutes prior to the harvesting time point (Figure S2C). As a control, we also performed iodoacetamide treatment and sequencing on unlabeled (no 4sU treatment) asynchronous G1 cells to provide an estimation of sequencing errors.

We filtered genes that contained at least 10 transcripts per million (TPM) and compared their new-to-total RNA (NTR) ratio. The replicate experiments were similar to each other (Figure S2D). We found a low level of new transcription in 90m G1 cells (transcription occurring between 30 and 90 minutes after release from nocodazole) which was significantly (p-value $< 2.2e^{-16}$) increased in the 180m G1 cells (transcription occurring between 120 and 180 minutes after nocodazole release) (Figure 2E, left) while the global transcript levels remained similar (Figure 2E, right). The amount of new transcription is lowest in early G1 followed by later G1 cells and the asynchronous G1 cells are most transcriptionally active (Figure 2E). Further, the expression of select cell cycle related genes (e.g., *CDT1*, *CDK4*, *CDK6*, and *PCNA*) was not prominent in 90m G1 samples, but was more apparent in 180m G1 and asynchronous G1 samples (Figure S2E). These results are consistent with previous reports that indicate that transcription progressively increases in post-mitotic G1 (Hsiung et al., 2016; Palozola et al., 2017). Taken together, these results show that the 90m G1 fraction contained cells in early G1 with condensed chromatin and low transcription, while the 180m G1 fraction contained cells from a later stage of G1 with increased transcriptional activity.

Identification of chromatin regions that interact with NL as cells progress through G1 phase

To identify chromatin sites that interact with the NL in early and later G1 phase cells, we used cTSA-seq to map lamin-B1 interacting chromatin in 90m G1 and 180m G1 HCT116 cells. For comparison, we also performed cTSA-seq of asynchronous G1, S, and G2 cells isolated by FACS. We refer to the G2/M population simply as “G2” since mitotic cells possess a disassembled nuclear envelope, and do not contribute much to the LADs signal (Kind et al., 2013; Moir et al., 2000a). Lamin-B1 cTSA-seq mapping revealed that NL-genome interactions occurred at the telomeric ends of chromosomes in 90m G1 HCT116 cells (Figure 3A). In the later G1 180m population, the NL-chromatin association at the chromatin ends was reduced, which was accompanied by the appearance of LADs throughout chromosomes that were similar to LADs seen in the asynchronous G1, S and G2 HCT116 cells (Figure 3A). The average lamin-B1 cTSA-seq signal of 90m G1 cells showed a lower Pearson correlation (< 0.5), while the signal from the 180m G1 cells was better correlated with the asynchronous G1, S, and G2 cells (Pearson > 0.7). The extensively studied human chromosomes 18 and 19 are known to preferentially localize to the nuclear periphery and nucleoplasm, respectively (Croft et al., 1999). We found that in the 90m early G1 cells, chromosome 18 shows an accumulation of lamin-B1 signal at one end of the chromosome while chromosome 19 shows little to no distal signal (Figure 3B). The differential localization of these chromosomes could contribute to the presence and absence of distal lamin-B1 signal seen during early G1.

The distal enrichment of lamin-B1 signal revealed by cTSA-seq in 90m early G1 cells occurred across metacentric, sub-metacentric and acrocentric chromosomes (Figure 3C, grey bars). The short, non-acrocentric chromosomes such as chromosomes 12,16-20 had early 90m G1 distal lamin-B1 signal that was mainly found only on the long arm of the chromosome (Figure 3D, blue bars). We also note that the short arm of these chromosomes, which showed little or no lamin-B1 signal, underwent a further reduction of signal in later 180m G1 and asynchronous G1 cells (Figure 3D, pink bars). We observed a similar dynamic lamin-B1-chromatin interaction in early and later G1 hTERT-RPE-1 cells (Figure S3A, S3B); however, the distal enrichment of LADs signal persisted longer than that observed for HCT116 cells, and is consistent with their slower progression from nocodazole block (Figure S3A, S3B).

As previously described (Tran et al., 2020; van Schaik et al., 2019), the vast majority of LADs mapped by cTSA-seq here were stable across the G1, S and G2 stages of the cell cycle (Figure 3A, 3B). This was also observed using both the GM12878 cell line and wild-type mouse embryonic stem cells (mESCs) (Figure S3C). Similar to what we previously described using the APEX2-ID, HMM defined cTSA-seq-mapped LADs from G1, S and G2 HCT116 cell populations possessed minor variation ("variable") in LADs that were H3K27me3 enriched and low in lamin-B1 signal while "shared" LADs which were stable across the cell cycle were high in both H3K9me3 and lamin-B1 signal (Figure S3D).

The number of genes (~5000) in chromatin regions that show preferential interaction with lamin-B1 based on cTSA-seq in the 90m early G1 cells was over twice the number of those (~2000) seen in later 180m G1, and the asynchronous G1, S and

G2 cells (Figure 3E). This is consistent with the fact that established LAD regions formed in interphase are relatively gene poor. Taken together, cTSA-seq mapping of cells from early and later G1 reveals a dynamic NL-chromatin interactions starting near the ends of chromosomes that eventually re-organize into the LAD patterns that are largely invariant during the rest of the cell cycle.

The NL-chromatin interaction patterns observed in early G1 cells are similar to those found in the oncogene-induced senescence cells

During organism development, different cell lineages assume different 3D genome architecture and LAD profiles to support different gene expression programs and cell functions (Kim et al., 2012; Peric-Hupkes and van Steensel, 2010). The same cell type may also have different genome organization and LAD profiles depending on whether they are in the state of quiescence or senescence (Bridger et al., 2000; Freund et al., 2012; Lenain et al., 2017; Sadaie et al., 2013; Shimi et al., 2011). Quiescence and senescence are often linked to the G1 phase of the cell (Afshari et al., 1993; Polymenis and Kennedy, 2017), but it remains unknown whether the unique genome organization of these cell states is related to G1 phase chromatin reorganization. To explore this, we first examined LADs mapped by DamID in Oncogene-Induced Senescence (OIS) Tig3 human fibroblasts (Lenain et al., 2017). As previously described, these $BRAF^{V600E}$-induced OIS LADs were different than LADs mapped in control cells (Figure 4A). We found that the OIS LADs were visually similar to those mapped in the 90m early G1 cells we mapped here across many chromosomes (Figure 4A) with the only notable exceptions on chromosomes 19 and 20. We note that LADs in

180m G1 and asynchronous G1, S, and G2 HCT116 cells are quite different from the control Tig3 cells as they are different cell types. We further quantified the enrichment of OIS LADs profile across sub-, metacentric and acrocentric chromosomes and found a bias for NL interactions toward chromosome ends (Figure 4B) that was similar to what we observed for LADs mapped in the 90m G1 cells (Figure 3B). A second study examining RAS^{V12}-induced OIS in IMR90 cells also noted a reduction of lamin-B1 chromatin immunoprecipitation (ChIP)-seq signal in the central region of chromosomes (Figure 4C) (Sadaie et al., 2013). We quantified this and also observed a modest increase in lamin-B1 ChIPseq signal toward the end of chromosomes in RAS^{V12}-induced OIS IMR90 cells (Figure 4D). The signal at the distal ends of chromosomes was significantly different in early G1 (90m G1) data when compared to both later G1 (180m G1) and asynchronous G1 samples, and between the control and OIS samples from the senescence studies (Figure 4E). These findings suggest that the early G1 genome organization may be a divergence point where the genome adopts a configuration for cell proliferation or senescence.

Temporal genome mapping methods offer us the ability to examine the dynamic properties of LADs. Here, we developed a method based on the TSA-seq method, which we call cTSA-seq. We found that the cTSA-seq method maps most LADs (>97%) identified by TSA-seq. The increased sensitivity of cTSA-seq offers an advantage over TSA-seq in mapping LADs in significantly lower numbers of cells. By combining mitotic block-release, FACS, and SLAM-seq, we are able to isolate early G1 phase cells that just begin gene expression and later G1 phase cells which exhibit increased gene expression. The application of lamin-B1 cTSA-seq to these populations enabled us to

identify dynamic NL-chromatin interactions during G1 progression where the distal ends of the post-mitotic chromosome initially interact with the NL in early G1 prior to the formation of relatively stable LADs shown by previous studies in proliferating human cells. This work expands upon previous imaging studies that show that telomeres preferentially localized to the NL in early G1 prior to moving to the nucleoplasm (Crabbe et al., 2012), and the movement of some LADs toward the NL during G1 (Kind et al., 2013; Luperchio et al., 2018). Further, our work is consistent with the reported dynamism of chromosome territories in early G1 where the movement of certain chromosomal loci (e.g., 5p14) toward the nuclear periphery occurs in early G1 (Thomson et al., 2004; Walter et al., 2003) and the loading of lamin-B1 onto the periphery of telophase chromosomes (Dechat et al., 2004; Haraguchi et al., 2008).

How each chromosome is positioned within the assemblage of mitotic chromosomes remains unclear. The differences in NL-chromatin interaction mapped by lamin-B1 cTSA-seq in early and later G1 human cells suggests that chromosomes are arranged with their distal ends at the exterior of the assemblage and thus facing the NL in early G1. This hints at the location of chromosomes and chromatin regions in late mitosis. Further efforts at exploring the rearrangements of NL-chromatin interactions should increase our understanding of mitotic chromosome organization and the subsequent steps of de-condensation during G1 nuclear reassembly.

The strong interaction between lamin-B1 and chromatin toward the ends of chromosomes seen in the early G1 cells were similar to LAD profiles mapped in the $BRAF^{V600E}$- and RAS^{V12}-induced OIS (Lenain et al., 2017; Sadaie et al., 2013), which is a hypertrophic proliferation-arrested cell state that occurs after the cell quiescence

restriction point (Blagosklonny, 2006). Previous studies of 3D genome organization in senescent cells showed a large scale switching of A and B compartments (Chandra et al., 2015; Criscione et al., 2016), which supports our current finding of NL-chromatin rearrangement. The inappropriate chromatin decondensation and/or inability to establish LADs may result in the senescence genome with abnormal epigenome modification and gene expression. Interestingly, senescence cells progressively reduce lamin-B1 protein (Freund et al., 2012; Shimi et al., 2011). It would be interesting to understand whether lamin-B1 reduction could contribute to the genome organization defects in OIS cells or senescence cells in general. Our results suggest that the OIS LAD profiles can be built upon the early G1 NL-chromatin interactions and it opens up new avenues to further study how different cell states, such as senescence and quiescence, develop different genome organizations.

Acknowledgements

We thank members of the Zheng and Goldman labs for advice and discussions. We also thank Allison Pinder, Frederick Tan and Xiaobin Zheng for their help with sequencing and data analysis. This study was funded by NIH NIGMS (GM106023) to Drs. Robert Goldman and Yixian Zheng and NIH NIGMS (GM110151) to Yixian Zheng. The authors declare no competing financial interests.

Author contributions

J.R. Tran designed, performed and interpreted experiments. S.A. Adam, R.D. Goldman and Y. Zheng participated in the design of the study. R.D. Goldman and Y. Zheng were responsible for project funding. J.R. Tran and Y. Zheng co-wrote the manuscript. All authors participated in revisions of the manuscript.

Figure legends

Figure 1: The cTSA-seq method maps NL-chromatin interactions

(A) The cTSA-seq experimental pipeline used in this study. **(B)** The lamin-B1 cTSA-seq reaction done with or without hydrogen peroxide after staining for the secondary-HRP antibody using K562 cells. Staining was done with Streptavidin (green) to highlight biotinylated material and a secondary antibody toward the lamin-B1 antibody (red). **(C)** UCSC Genome browser view of lamin-B1 cTSA-seq mapping profile in the K562 cells (hg19, Chr1, left). Previously published APEX2-ID, DamID and TSA-seq mapping profiles from K562 cells are shown for comparison. The y-axis represents a z-score. Pearson correlation matrix for DamID, TSA-seq, APEX2-ID and cTSA-seq mapped DNA (right).

Figure S1: Additional controls for cTSA-seq labeling, measurements of labeling diffusion and observed variations in K562 LADs

Example images for lamin-B1 cTSA-seq reaction in **(A)** HCT116 cells using an anti-rabbit HRP or an anti-mouse HRP secondary and **(B)** in wild-type or lamin-B1 null MEFs. Staining was done with Streptavidin (green) and lamin-B1 (red). **(C)** The observed diffusion of labeling from the lamin-B1 signal is presented as a boxplot. **(D)** Scatterplot of K562 cTSA-seq replicate mapping data (n=2, z-score). Pearson correlation of 0.93 was calculated for the K562 cTSA-seq replicates.

Figure 2: Isolation and characterization of synchronous early and later G1 cells

(A) Illustration of experimental protocol for nocodazole block and release. **(B)** Typical FACS profiles showing the time course of emergence of G1 cells after washing out nocodazole. DNA was stained with Hoechst 33342 prior to FACS. Asynchronous populations ("Async") were used as a gating reference. **(C)** Lamin-B1 immunostaining (green) for early G1 cells (90m G1), later G1 cells (180m G1) and asynchronous G1 cells (Async G1) isolated from asynchronous cell cultures. DAPI is presented in grayscale. **(D)** Look up table (LUT) display, which reflects intensity of DAPI signal (DNA) for early G1 (90m G1), later G1 (180m G1) and asynchronous G1 (Async G1) (left). Graph showing the percentage of cells containing apparently condensed chromatin in 90m G1 and 180m G1 populations (right). **(E)** Boxplots showing the new transcripts to all transcripts ratio (NTR, left) and the transcripts per million (TPM, right) observed for different samples as indicated. P-values shown in the right boxplot were calculated from a two-tailed t-test.

Figure S2: Isolation and characterization of early and later G1 hTERT-RPE1 cells and SLAM-seq analyses of HCT116 cells.

(A) Typical FACS mitotic release profile for hTERT-RPE1 cells. The Asynchronous cell population ("Async") was used as a gating reference. **(B)** Lamin-B1 immunostaining for hTERT-RPE1 cells. Lamin-B1 is presented in green and DNA (DAPI) is presented as

grayscale. **(C)** Experimental pipeline for performing SLAM-seq experiments in early (90m) and later (180m) G1 HCT116 cells. **(D)** Scatterplots of SLAM-seq biological replicates (n=2) for untreated asynchronous G1 (Async G1 no 4sU), 90m G1, 180m G1 and asynchronous G1 (Async G1) HCT116 cells. The blue dashed line is a reference diagonal line and the red line represents a linear model. **(E)** Heatmap showing the new transcription level for select genes encoding known cell cycle proteins or from histone gene clusters in the indicated cell populations. Note that the asynchronous G1 with no 4sU is labeled as “no 4sU”.

Figure 3: Lamin-B1 cTSA-seq reveals NL-chromatin interaction near chromosome ends in early G1 HCT116 cells

(**A**) UCSC Genome browser tracks (hg19) mapped by lamin-B1 cTSA-seq from early G1 (90m G1), later G1 (180m G1), asynchronous G1, S and G2 sorted HCT116 cells. Metacentric chromosome 1 (top) and acrocentric chromosome 14 (bottom) are displayed. The data presented are average z-scores of both replicate experiments. (**B**) UCSC genome browser tracks of lamin-B1 cTSA-seq for chromosomes 18 (top) and 19 (bottom). The data presented are average z-scores of both replicate experiments. (**C**) Average lamin-B1 cTSA-seq signal from meta- and submetacentric (left) and acrocentric (right) chromosomes in the indicated cell cycle stages. Chromosomes were segmented as a percentage of their length and the lamin-B1 signal was quantified over these windows. Error bars represent standard deviation of signal. Grey bars highlight regions where the signal changes in early G1. (**D**) The average lamin-B1 cTSA-seq signal for smaller (chromosomes 12, 16-20) meta- and submetacentric chromosomes. Red bars show low cTSA-seq signal that decreases further and blue bars show strong distal cTSA-seq signal that decreases. (**E**) Pie-charts showing the number of genes inside and outside of the lamin-B1 cTSA-seq mapped regions (all referred to as “In LAD” and “Outside LAD”, respective). Gene localization was called if at least 80% of the gene resided within the examined feature.

Figure S3: Lamin-B1 cTSA-seq mapping showing signals toward chromosome ends in early G1 hTERT-RPE1 cells

(A) UCSC genome browser tracks (chromosome 2, hg19) mapped by lamin-B1 cTSA-seq from 90m G1, 180m G1 and asynchronous G1 populations of hTERT-RPE1 cells. **(B)** Average lamin-B1 cTSA-seq signal from meta- and submetacentric (left) and acrocentric (right) hTERT-RPE1 chromosomes. Error bars represent standard deviation. Grey bars highlight regions where the signal changes during G1 progression. **(C)** Lamin-B1 cTSA-seq mapping in G1, S, and G2 cells FACS isolated from asynchronously growing GM12878 (top) and wild-type mESCs (bottom). **(D)** Boxplot showing the ENCODE HCT116 epigenetic ChIPseq signal quantified over cTSA-seq mapped LADs that were shared (top panel) or variable (middle panel) during in G1, S, and G2 of the cell cycle. Boxplot showing the change in lamin-B1 cTSA-seq signal in shared and variable LADs over the cell cycle (bottom panel).

Figure 4: Early G1 NL-chromatin interactions identified by lamin-B1 cTSA-seq are similar to LADs identified in Oncogene-Induced Senescence (OIS) cells

(**A**) UCSC Genome browser tracks (hg19) of LADs mapped by lamin-B1 DamID from control and Oncogene-induced senescence (OIS) human Tig3 cells (Lenain et al., 2017) and by lamin-B1 cTSA-seq from 90m G1, 180m G1, G1, S and G2 HCT116 cells. Metacentric (chr 7), acrocentric (chr 14) and small metacentric (chr 18) chromosomes are shown. The cTSA-seq data presented are average z-scores of both replicate experiments. (**B**) Plots displaying the average lamin-B1 DamID signal from control and OIS Tig3 cells. Meta- and submetacentric (left) and acrocentric (right) chromosomes are shown, and the error bars represent standard deviation. Grey bars highlight regions where the signal changes in OIS cells. (**C**) UCSC Genome browser tracks of lamin-B1 ChIP-seq signal (hg19) in control and OIS IMR90 human cells for chromosomes 5, 8 and 12 (Sadaie, et al., 2013). (**D**) Plots displaying the average lamin-B1 ChIP-seq signal from control and OIS IMR90 cells (Sadaie, et al., 2013). Grey bars highlight regions where the signal changes in OIS cells. (**E**) Average HCT116 lamin-B1 cTSA-seq signal measured from the ends of chromosomes for 90m G1, 180m G1, asynchronous G1. The control ("ctrl") and OIS data are from Lenain et al., 2017 and Sadaie, et al., 2013. We defined the chromosome ends as the last 2.5% of each chromosome arm. P-values represent a two-tailed t-test and error bars represent the standard deviation.

References

Afshari, C.A., P.J. Vojta, L.A. Annab, P.A. Futreal, T.B. Willard, and J.C. Barrett. 1993. Investigation of the role of G1/S cell cycle mediators in cellular senescence. *Exp Cell Res*. 209:231-237.

Belmont, A.S., and K. Bruce. 1994. Visualization of G1 chromosomes: a folded, twisted, supercoiled chromonema model of interphase chromatid structure. *J Cell Biol*. 127:287-302.

Blagosklonny, M.V. 2006. Cell senescence: hypertrophic arrest beyond the restriction point. *J Cell Physiol*. 209:592-597.

Bridger, J.M., S. Boyle, I.R. Kill, and W.A. Bickmore. 2000. Re-modelling of nuclear architecture in quiescent and senescent human fibroblasts. *Curr Biol*. 10:149-152.

Chandra, T., P.A. Ewels, S. Schoenfelder, M. Furlan-Magaril, S.W. Wingett, K. Kirschner, J.Y. Thuret, S. Andrews, P. Fraser, and W. Reik. 2015. Global reorganization of the nuclear landscape in senescent cells. *Cell Rep*. 10:471-483.

Chen, Y., Y. Zhang, Y. Wang, L. Zhang, E.K. Brinkman, S.A. Adam, R. Goldman, B. van Steensel, J. Ma, and A.S. Belmont. 2018. Mapping 3D genome organization relative to nuclear compartments using TSA-Seq as a cytological ruler. *J Cell Biol*. 217:4025-4048.

Chubb, J.R., S. Boyle, P. Perry, and W.A. Bickmore. 2002. Chromatin motion is constrained by association with nuclear compartments in human cells. *Curr Biol*. 12:439-445.

Crabbe, L., A.J. Cesare, J.M. Kasuboski, J.A. Fitzpatrick, and J. Karlseder. 2012. Human telomeres are tethered to the nuclear envelope during postmitotic nuclear assembly. *Cell Rep*. 2:1521-1529.

Criscione, S.W., M. De Cecco, B. Siranosian, Y. Zhang, J.A. Kreiling, J.M. Sedivy, and N. Neretti. 2016. Reorganization of chromosome architecture in replicative cellular senescence. *Sci Adv*. 2:e1500882.

Croft, J.A., J.M. Bridger, S. Boyle, P. Perry, P. Teague, and W.A. Bickmore. 1999. Differences in the localization and morphology of chromosomes in the human nucleus. *J Cell Biol*. 145:1119-1131.

Dechat, T., A. Gajewski, B. Korbei, D. Gerlich, N. Daigle, T. Haraguchi, K. Furukawa, J. Ellenberg, and R. Foisner. 2004. LAP2alpha and BAF transiently localize to telomeres and specific regions on chromatin during nuclear assembly. *J Cell Sci*. 117:6117-6128.

Dolken, L. 2013. High resolution gene expression profiling of RNA synthesis, processing, and decay by metabolic labeling of newly transcribed RNA using 4-thiouridine. *Methods Mol Biol*. 1064:91-100.

Dou, Z., C. Xu, G. Donahue, T. Shimi, J.A. Pan, J. Zhu, A. Ivanov, B.C. Capell, A.M. Drake, P.P. Shah, J.M. Catanzaro, M.D. Ricketts, T. Lamark, S.A. Adam, R. Marmorstein, W.X. Zong, T. Johansen, R.D. Goldman, P.D. Adams, and S.L. Berger. 2015. Autophagy mediates degradation of nuclear lamina. *Nature*. 527:105-109.

Erhard, F., M.A.P. Baptista, T. Krammer, T. Hennig, M. Lange, P. Arampatzi, C.S. Jurges, F.J. Theis, A.E. Saliba, and L. Dolken. 2019. scSLAM-seq reveals core features of transcription dynamics in single cells. *Nature*. 571:419-423.

Forsberg, F., A. Brunet, T.M.L. Ali, and P. Collas. 2019. Interplay of lamin A and lamin B LADs on the radial positioning of chromatin. *Nucleus*. 10:7-20.

Freund, A., R.M. Laberge, M. Demaria, and J. Campisi. 2012. Lamin B1 loss is a senescence-associated biomarker. *Mol Biol Cell*. 23:2066-2075.

Guelen, L., L. Pagie, E. Brasset, W. Meuleman, M.B. Faza, W. Talhout, B.H. Eussen, A. de Klein, L. Wessels, W. de Laat, and B. van Steensel. 2008. Domain organization of human chromosomes revealed by mapping of nuclear lamina interactions. *Nature*. 453:948-951.

Haraguchi, T., T. Kojidani, T. Koujin, T. Shimi, H. Osakada, C. Mori, A. Yamamoto, and Y. Hiraoka. 2008. Live cell imaging and electron microscopy reveal dynamic processes of BAF-directed nuclear envelope assembly. *J Cell Sci*. 121:2540-2554.

Haraguchi, T., T. Koujin, M. Segura-Totten, K.K. Lee, Y. Matsuoka, Y. Yoneda, K.L. Wilson, and Y. Hiraoka. 2001. BAF is required for emerin assembly into the reforming nuclear envelope. *J Cell Sci*. 114:4575-4585.

Herzog, V.A., B. Reichholf, T. Neumann, P. Rescheneder, P. Bhat, T.R. Burkard, W. Wlotzka, A. von Haeseler, J. Zuber, and S.L. Ameres. 2017. Thiol-linked alkylation of RNA to assess expression dynamics. *Nat Methods*. 14:1198-1204.

Hsiung, C.C., C.R. Bartman, P. Huang, P. Ginart, A.J. Stonestrom, C.A. Keller, C. Face, K.S. Jahn, P. Evans, L. Sankaranarayanan, B. Giardine, R.C. Hardison, A. Raj, and G.A. Blobel. 2016. A hyperactive transcriptional state marks genome reactivation at the mitosis-G1 transition. *Genes Dev*. 30:1423-1439.

Jurges, C., L. Dolken, and F. Erhard. 2018. Dissecting newly transcribed and old RNA using GRAND-SLAM. *Bioinformatics*. 34:i218-i226.

Kim, Y., K. McDole, and Y. Zheng. 2012. The function of lamins in the context of tissue building and maintenance. *Nucleus*. 3:256-262.

Kind, J., L. Pagie, H. Ortabozkoyun, S. Boyle, S.S. de Vries, H. Janssen, M. Amendola, L.D. Nolen, W.A. Bickmore, and B. van Steensel. 2013. Single-cell dynamics of genome-nuclear lamina interactions. *Cell*. 153:178-192.

Lenain, C., C.A. de Graaf, L. Pagie, N.L. Visser, M. de Haas, S.S. de Vries, D. Peric-Hupkes, B. van Steensel, and D.S. Peeper. 2017. Massive reshaping of genome-nuclear lamina interactions during oncogene-induced senescence. *Genome Res*. 27:1634-1644.

Li, G., G. Sudlow, and A.S. Belmont. 1998. Interphase cell cycle dynamics of a late-replicating, heterochromatic homogeneously staining region: precise choreography of condensation/decondensation and nuclear positioning. *J Cell Biol*. 140:975-989.

Luperchio, T.R., M.E.G. Sauria, V.E. Hoskins, X. Wong, E. Deboy, M.-C. Gaillard, P. Tsang, K. Pekrun, R.A. Ach, N.A. Yamada, J. Taylor, and K.L. Reddy. 2018. The repressive genome compartment is established early in the cell cycle before forming the lamina associated domains. *In* bioRxiv doi: https://doi.org/10.1101/481598.

Moir, R.D., T.P. Spann, R.I. Lopez-Soler, M. Yoon, A.E. Goldman, S. Khuon, and R.D. Goldman. 2000a. Review: the dynamics of the nuclear lamins during the cell cycle-- relationship between structure and function. *J Struct Biol*. 129:324-334.

Moir, R.D., M. Yoon, S. Khuon, and R.D. Goldman. 2000b. Nuclear lamins A and B1: different pathways of assembly during nuclear envelope formation in living cells. *J Cell Biol*. 151:1155-1168.

Palozola, K.C., G. Donahue, H. Liu, G.R. Grant, J.S. Becker, A. Cote, H. Yu, A. Raj, and K.S. Zaret. 2017. Mitotic transcription and waves of gene reactivation during mitotic exit. *Science*. 358:119-122.

Peric-Hupkes, D., and B. van Steensel. 2010. Role of the nuclear lamina in genome organization and gene expression. *Cold Spring Harb Symp Quant Biol*. 75:517-524.

Polymenis, M., and B.K. Kennedy. 2017. Unbalanced Growth, Senescence and Aging. *Adv Exp Med Biol*. 1002:189-208.

Sadaie, M., R. Salama, T. Carroll, K. Tomimatsu, T. Chandra, A.R. Young, M. Narita, P.A. Perez-Mancera, D.C. Bennett, H. Chong, H. Kimura, and M. Narita. 2013. Redistribution of the Lamin B1 genomic binding profile affects rearrangement of heterochromatic domains and SAHF formation during senescence. *Genes Dev*. 27:1800-1808.

Shimi, T., V. Butin-Israeli, S.A. Adam, R.B. Hamanaka, A.E. Goldman, C.A. Lucas, D.K. Shumaker, S.T. Kosak, N.S. Chandel, and R.D. Goldman. 2011. The role of nuclear lamin B1 in cell proliferation and senescence. *Genes Dev*. 25:2579-2593.

Thomson, I., S. Gilchrist, W.A. Bickmore, and J.R. Chubb. 2004. The radial positioning of chromatin is not inherited through mitosis but is established de novo in early G1. *Curr Biol*. 14:166-172.

Tran, J.R., D.I. Paulson, J.J. Moresco, S.A. Adam, J.R. Yates III, R.D. Goldman, and Y. Zheng. 2020. The versatility of Ascorbate Peroxidase-aided mapping uncovers insights of the nuclear lamina interactions and function. *bioRxiv 2020.02.05.935635; doi: https://doi.org/10.1101/2020.02.05.935635*.

van Schaik, T., M. Vos, D. Peric-Hupkes, and B. van Steensel. 2019. Cell cycle dynamics of lamina associated DNA. *bioRxiv*:2019.2012.2019.881979.

Walter, J., L. Schermelleh, M. Cremer, S. Tashiro, and T. Cremer. 2003. Chromosome order in HeLa cells changes during mitosis and early G1, but is stably maintained during subsequent interphase stages. *J Cell Biol*. 160:685-697.

Zhang, L., Y. Zhang, Y. Chen, O. Gholamalamdari, J. Ma, and A.S. Belmont. 2019. TSA-Seq 2.0 reveals both conserved and variable chromosomal distances to nuclear speckles. *bioRxiv*:824433.

Zhang, L., Y. Zhang, Y. Chen, O. Gholamalamdari, Y. Wang, J. Ma, and A.S. Belmont. 2020. TSA-seq reveals a largely conserved genome organization relative to nuclear speckles with small position changes tightly correlated with gene expression changes. *Genome Res*.

Figure 1

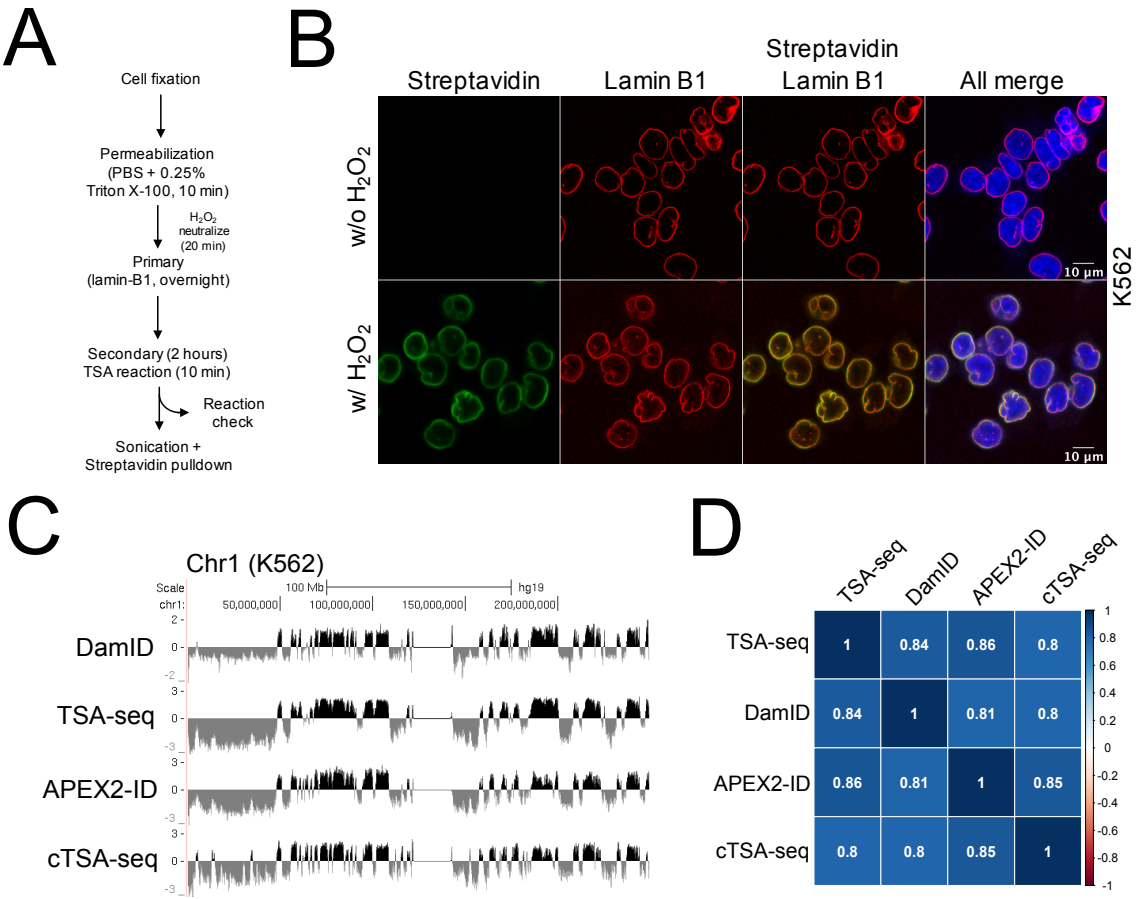
A
Cell fixation
Permeabilization
(PBS + 0.25%
Triton X-100, 10 min)
H_2O_2
neutralize
(20 min)
Primary
(lamin-B1, overnight)
Secondary (2 hours)
TSA reaction (10 min)
Reaction
check
Sonication +
Streptavidin pulldown
B
Streptavidin
Lamin B1
Streptavidin
Lamin B1
All merge
w/o H_2O_2
w/ H_2O_2
10 µm
10 µm
K562
C
Chr1 (K562)
Scale
chr1:
100 Mb
hg19
50,000,000
100,000,000
150,000,000
200,000,000
DamID
TSA-seq
APEX2-ID
cTSA-seq
D
TSA-seq
DamID
APEX2-ID
cTSA-seq
TSA-seq 1 0.84 0.86 0.8
DamID 0.84 1 0.81 0.8
APEX2-ID 0.86 0.81 1 0.85
cTSA-seq 0.8 0.8 0.85 1
1
0.8
0.6
0.4
0.2
0
-0.2
-0.4
-0.6
-0.8
-1

Figure 2

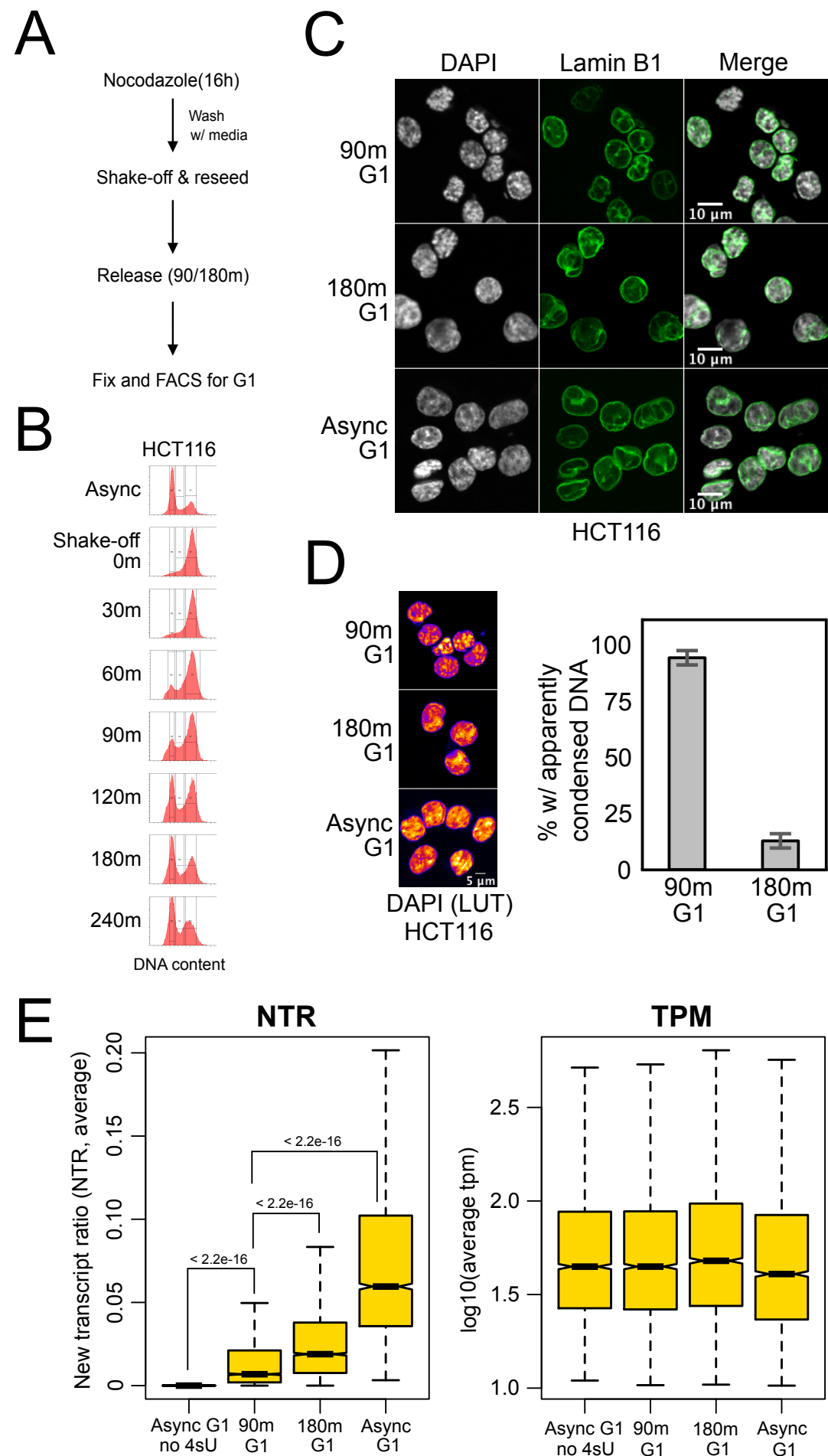
A
Nocodazole(16h)
Wash w/ media
Shake-off & reseed
Release (90/180m)
Fix and FACS for G1
B
HCT116
Async
Shake-off 0m
30m
60m
90m
120m
180m
240m
DNA content
C
DAPI
Lamin B1
Merge
90m G1
180m G1
Async G1
10 µm
HCT116
D
90m G1
180m G1
Async G1
5 µm
DAPI (LUT)
HCT116
% w/ apparently condensed DNA
100
75
50
25
0
90m G1
180m G1
E
NTR
New transcript ratio (NTR, average)
0
0.05
0.10
0.15
0.20
< 2.2e-16
< 2.2e-16
< 2.2e-16
Async G1 no 4sU
90m G1
180m G1
Async G1
TPM
log10(average tpm)
1.0
1.5
2.0
2.5
Async G1 no 4sU
90m G1
180m G1
Async G1

Figure 3

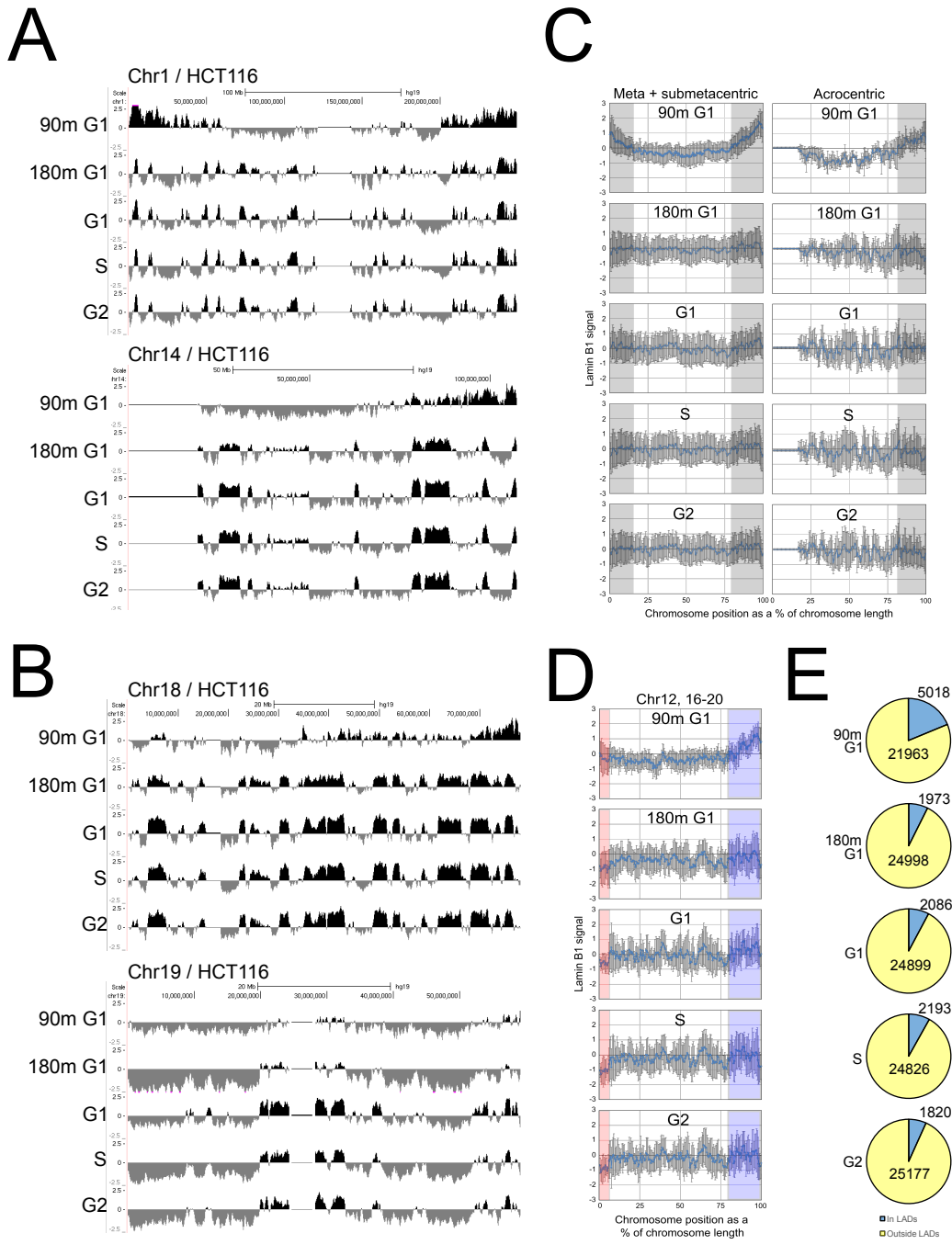
A
Chr1 / HCT116
90m G1
180m G1
G1
S
G2
Chr14 / HCT116
90m G1
180m G1
G1
S
G2
B
Chr18 / HCT116
90m G1
180m G1
G1
S
G2
Chr19 / HCT116
90m G1
180m G1
G1
S
G2
C
Meta + submetacentric
Acrocentric
90m G1
180m G1
G1
S
G2
Lamin B1 signal
Chromosome position as a % of chromosome length
D
Chr12, 16-20
90m G1
180m G1
G1
S
G2
Lamin B1 signal
Chromosome position as a % of chromosome length
E
90m G1
5018
21963
180m G1
1973
24998
G1
2086
24899
S
2193
24826
G2
1820
25177
In LADs
Outside LADs

Figure 4

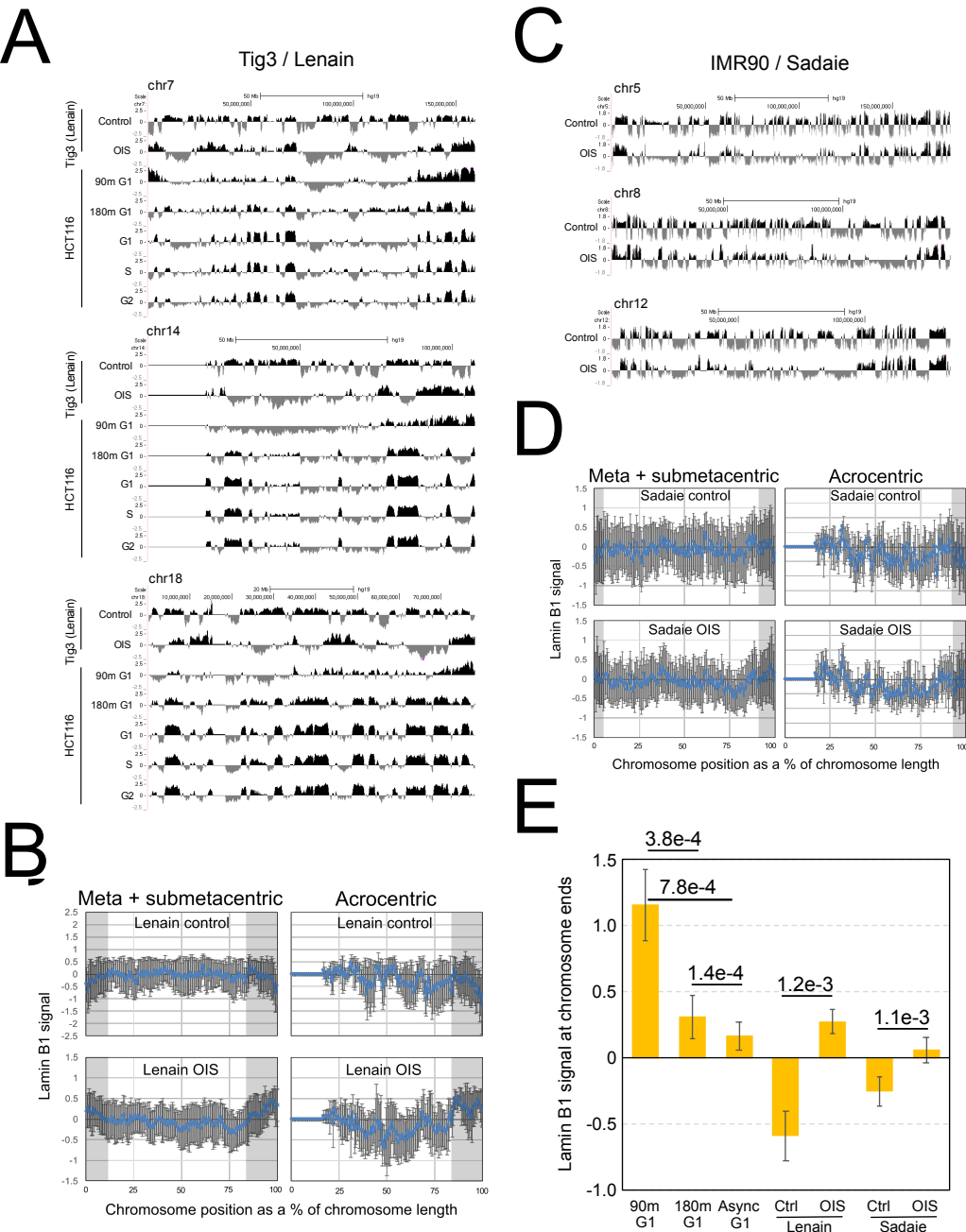
A
Tig3 / Lenain
chr7
chr14
chr18
Tig3 (Lenain)
HCT116
Control
OIS
90m G1
180m G1
G1
S
G2
B
Meta + submetacentric
Acrocentric
Lenain control
Lenain OIS
Lamin B1 signal
Chromosome position as a % of chromosome length
C
IMR90 / Sadaie
chr5
chr8
chr12
D
Sadaie control
Sadaie OIS
E
3.8e-4
7.8e-4
1.4e-4
1.2e-3
1.1e-3
Lamin B1 signal at chromosome ends
90m G1
180m G1
Async G1
Ctrl
OIS
Lenain
Sadaie

Figure S1

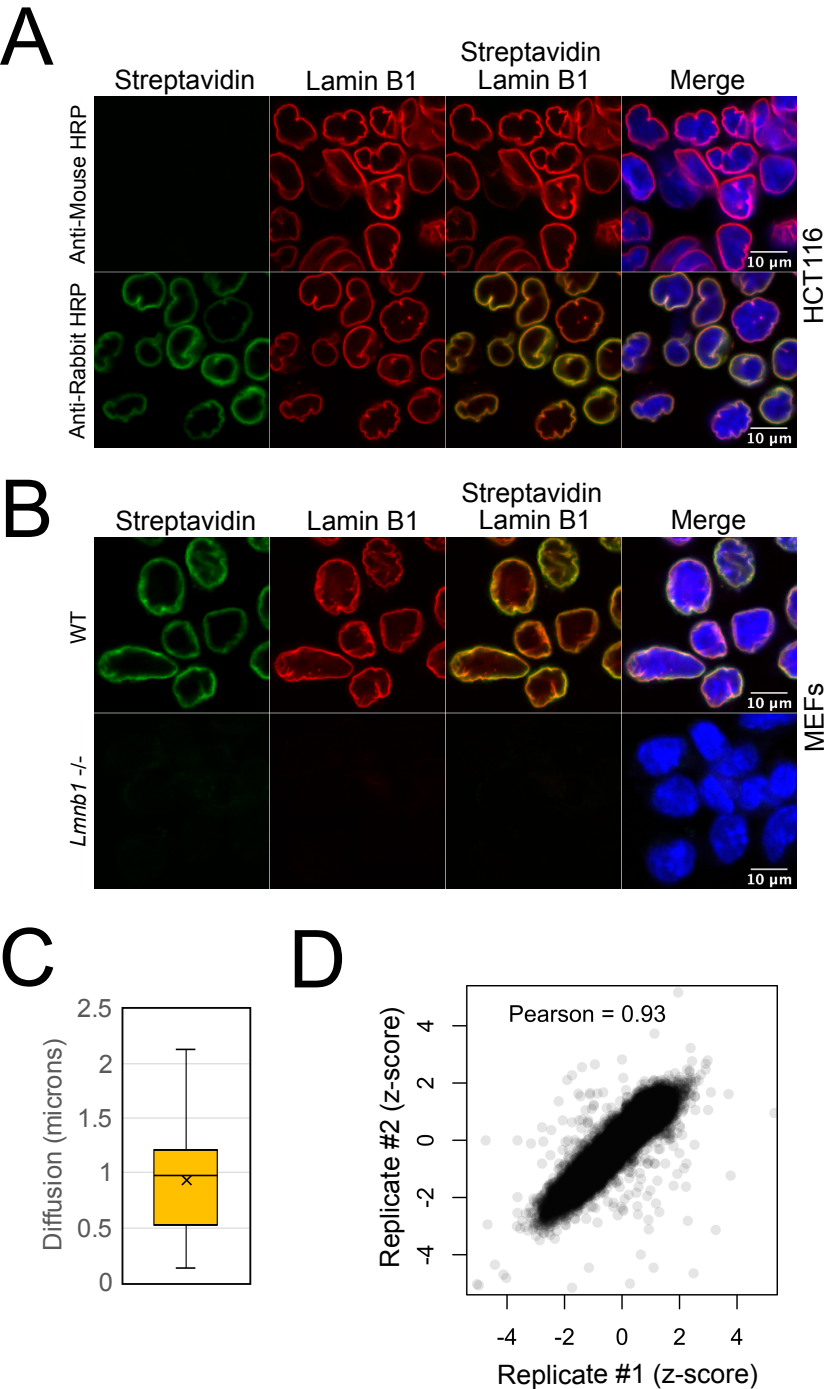
A
Streptavidin
Lamin B1
Streptavidin
Lamin B1
Merge
Anti-Mouse HRP
Anti-Rabbit HRP
HCT116
10 µm
10 µm
B
Streptavidin
Lamin B1
Streptavidin
Lamin B1
Merge
WT
Lmnb1 -/-
MEFs
10 µm
10 µm
C
Diffusion (microns)
2.5
2
1.5
1
0.5
0
D
Pearson = 0.93
Replicate #2 (z-score)
Replicate #1 (z-score)
-4
-2
0
2
4

Figure S2

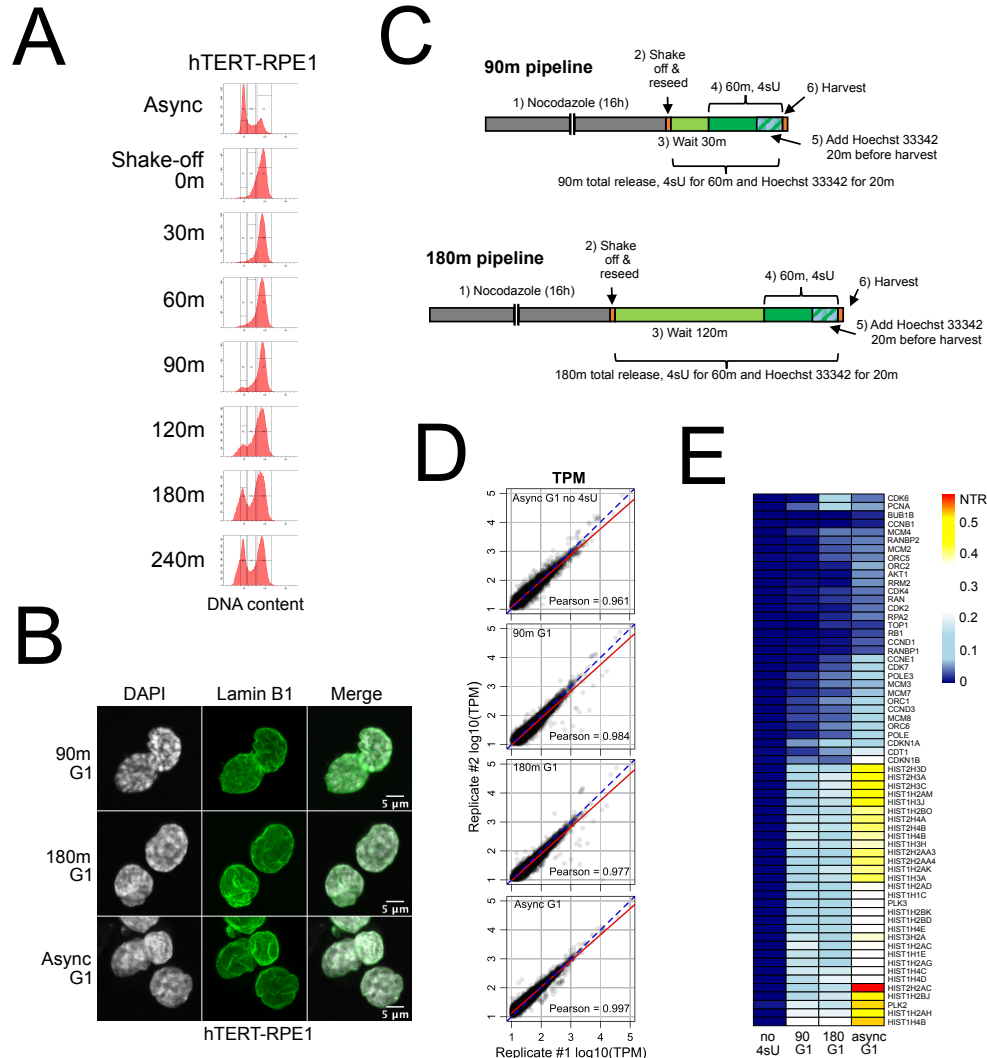
A
hTERT-RPE1
Async
Shake-off 0m
30m
60m
90m
120m
180m
240m
DNA content
B
DAPI
Lamin B1
Merge
90m G1
180m G1
Async G1
5 µm
hTERT-RPE1
C
90m pipeline
1) Nocodazole (16h)
2) Shake off & reseed
3) Wait 30m
4) 60m, 4sU
5) Add Hoechst 33342 20m before harvest
6) Harvest
90m total release, 4sU for 60m and Hoechst 33342 for 20m
180m pipeline
1) Nocodazole (16h)
2) Shake off & reseed
3) Wait 120m
4) 60m, 4sU
5) Add Hoechst 33342 20m before harvest
6) Harvest
180m total release, 4sU for 60m and Hoechst 33342 for 20m
D
TPM
Async G1 no 4sU
Pearson = 0.961
90m G1
Pearson = 0.984
180m G1
Pearson = 0.977
Async G1
Pearson = 0.997
Replicate #2 log10(TPM)
Replicate #1 log10(TPM)
E
NTR
no 4sU
90 G1
180 G1
async G1
CDK6
PCNA
BUB1B
CCNB1
MCM4
RANBP2
MCM2
ORC5
ORC2
AKT1
RRM2
CDK4
RAN
CDK2
RPA2
TOP1
RB1
CCND1
RANBP1
CCNE1
CDK7
POLE3
MCM3
MCM7
ORC1
CCND3
MCM8
ORC6
POLE
CDKN1A
CDT1
CDKN1B
HIST2H3D
HIST2H3A
HIST2H3C
HIST1H2AM
HIST1H3J
HIST1H2BO
HIST2H4A
HIST2H4B
HIST1H4B
HIST1H3H
HIST2H2AA3
HIST2H2AA4
HIST1H2AK
HIST1H3A
HIST1H2AD
HIST1H1C
PLK3
HIST1H2BK
HIST1H2BD
HIST1H4E
HIST3H2A
HIST1H2AC
HIST1H1E
HIST1H2AG
HIST1H4C
HIST1H4D
HIST2H2AC
HIST1H2BJ
PLK2
HIST1H2AH
HIST1H4B

Figure S3

A

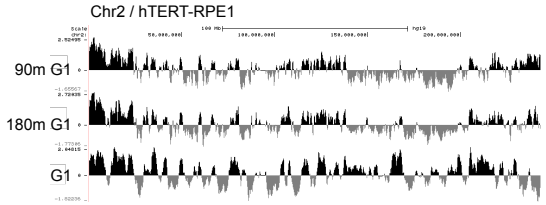

B

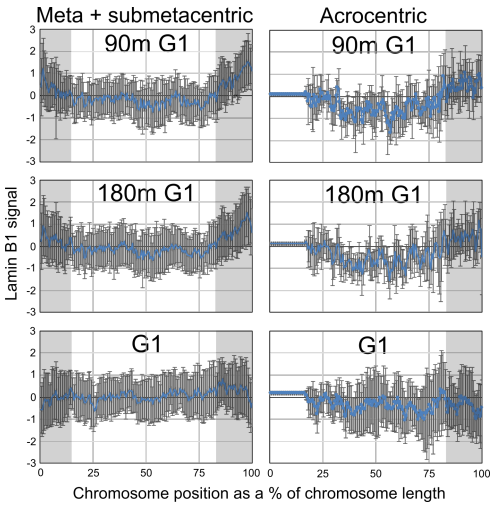

C

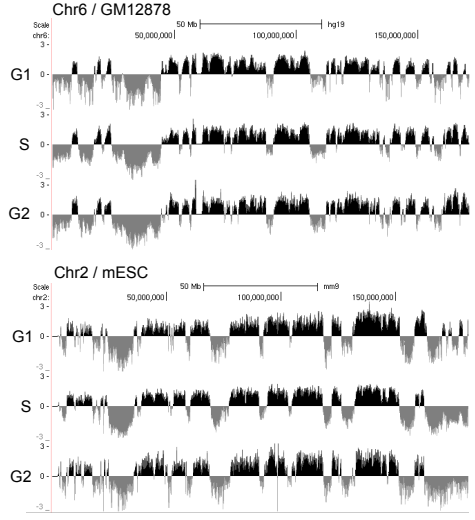
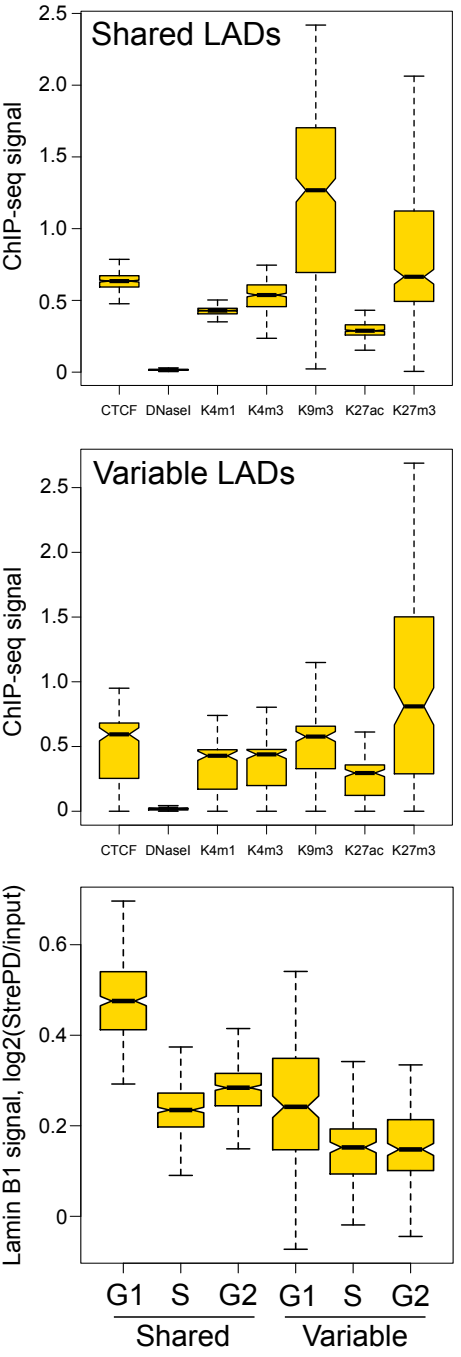
D